A&A, 689, A17 (2024)
https://doi.org/10.1051/0004-6361/202450909

Astronomy & Astrophysics

Low-velocity streams inside the planetary nebula H 2-18

A 3D photoionisation and kinematical reconstruction⋆

K. Gesicki[1,⋆⋆], A. Zijlstra[2,3], M. Hajduk[4], A. Iwanowska[1], K. Grzesiak[1], K. Lisiecki[1], and J. Lipinski[1]

[1] Institute of Astronomy, Faculty of Physics, Astronomy and Informatics, Nicolaus Copernicus University, ul. Grudziadzka 5, 87-100 Torun, Poland
[2] Jodrell Bank Centre for Astrophysics, School of Physics & Astronomy, University of Manchester, Oxford Road, Manchester M13 9PL, UK
[3] School of Mathematical and Physical Sciences, Macquarie University, Sydney, NSW 2109, Australia
[4] Department of Geodesy, Faculty of Geoengineering, University of Warmia and Mazury, ul. Oczapowskiego 2, 10-719 Olsztyn, Poland

Received 29 May 2024 / Accepted 7 July 2024

ABSTRACT

Aims. Numerous planetary nebulae show complicated inner structures that are not obvious to explain. For one such object, we undertook a detailed 3D photoionisation and kinematical model analysis to gain a better understanding of the underlying shaping processes.
Methods. We obtained 2D ARGUS/IFU spectroscopy covering the whole nebula in selected representative emission lines. We used 3D photoionisation modelling to compute images and line profiles, and a comparison of the observations with the models was performed to fine-tune the model details. This procedure predicts the approximate nebular 3D structure and kinematics.
Results. We find that within a cylindrical outer nebula, there is a hidden, very dense bar-like or cylindrical inner structure. Both structures are co-axial and are inclined to the sky by 40 deg. We propose that the wide, asymmetric, one-sided plume is a flat structure attached to one end of the bar. All nebular components share the same kinematics, with an isotropic velocity field that monotonically increases with distance from the star before reaching a plateau. The relatively low velocities indicate that the observed shapes do not require particularly energetic processes, and there is no indication for the current presence of a jet. The 3D model reproduces the observed line ratios and the detailed structure of the object significantly better than previous models.

Key words. planetary nebulae: general – planetary nebulae: individual: H 2-18 (PN G 006.3+04.4)

1. Introduction

The theory of mass loss at the late asymptotic giant branch evolutionary phase is still in development, and it is one of the most important missing factors in stellar evolution theory. The ejected matter often take on interesting axisymmetric or asymmetric shapes, and the physical processes causing these effects are far from clear. Theoretical approaches need some suggestions and hints derived from observations, and such hints can be found from studies of planetary nebulae (PNe).

A classical concept of a PN is a shell of gas ejected by a star at the end of its life. Initially, the shell is opaque and hidden from view. Only after the shell expands sufficiently for the hot central core to shine through and ionise the nearby material does the object enter the PN phase. This phase ends when the ejecta expand to a large volume and very low density or when the remaining stellar core enters the white dwarf cooling track and fades significantly. The timescales of each are comparable.

We studied the details of PNe by applying the so-called kinematical reconstruction (sometimes referred to as a 'reverse engineering'). This derives the nebular structure and kinematics from line profiles based on assumed velocity fields that are verified through photoionisation and emission line profile computation (Gesicki & Zijlstra 2000). For this method to work and to reduce the inherent ambiguities, both high-quality images and high-resolution spectroscopy are needed in order to constrain the density and velocity spatial distributions.

In this work, we present new 2D spectroscopic observations and new 3D photoionisation modelling of a previously analysed PN. The modelling and observations allowed us to compare the new results with the older ones, to verify the new approach, and to indicate all of its advantages.

The planetary nebula H 2-18 (see Fig. 1) was previously analysed using the kinematical reconstruction approach. Gesicki et al. (2014) applied the Torun codes and derived a spherically symmetric model of this PN. Later, Gesicki et al. (2016) used the same observational data but applied the pseudo-3D code py-Cloudy. Both papers were based on HST imaging and ESO/VLT spectroscopic long-slit observations.

In 2017, we obtained ARGUS IFU 2D data of high spatial and spectral resolution of this object. The observations covered selected spectral lines of high and low excitation that probe different nebular regions, and they allowed for more precise kinematic and photoionisation analysis. The collected data are presented in Sect. 2.

For the modelling of this nebula, we applied the publicly available code MOCASSIN, which computes photoionisation of a 3D gaseous structure. To initiate the 3D modelling and to

⋆ Based on observations collected at the European Southern Observatory under ESO programme 099.D-0386(A).
⋆⋆ Corresponding author; kmgesicki@umk.pl

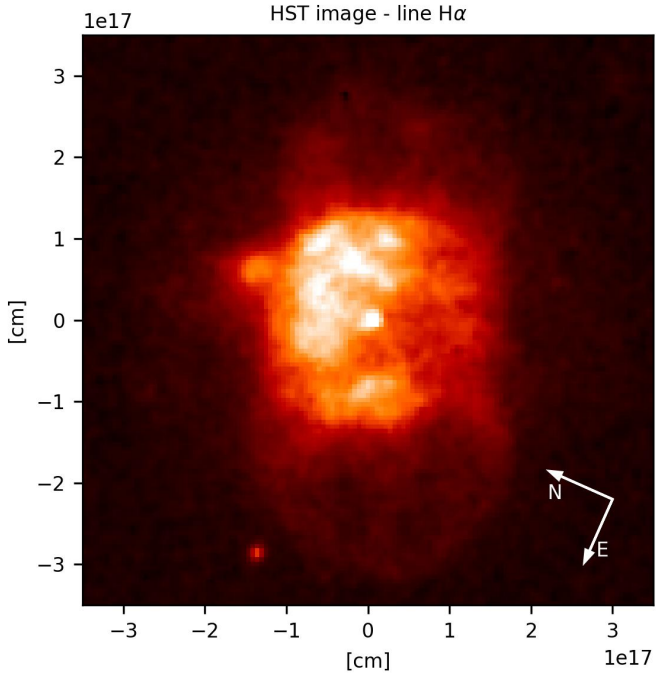

Fig. 1. *Hubble* Space Telescope image of PN H 2-18 obtained in an Hα filter. The plot is in linear intensity scale. The angular dimensions have been converted to 10^{17} cm while assuming that the PN is at the Galactic Bulge distance of 8 kpc and centred at the star position. The image has been rotated to compare it more easily with computed structures.

compare the model outputs with the 2D spectra, we wrote a number of Python scripts. The modelling procedure and the obtained density structure and velocity field are described in Sect. 3.

The nebula H 2-18 appears to be complex, and there are few published studies of similar objects to which it can be compared. The generalisation of our unique results is also not easy. Some aspects of this issue are discussed in Sect. 4.

2. Observations

The ESO FLAMES/ARGUS instrument provided high-resolution spectroscopy of the spatially resolved Galactic Bulge PN H 2-18 (PN G 006.3+04.4; 17:43:28.7, −21:09:51.30 (J2000)). The nebula was observed in 2017 on September 18 (wavelengths around 465 and 504 nm) and September 21 (627 and 651 nm). The wide field of view is a mosaic of 22 × 14 microlenses, each of 0.52 × 0.52 arcsec. The instrument setup was selected to cover the regions around four lines at a high-spectral resolution ($R \gtrsim 30\,000$), namely [O III] 500.7 nm, Hα (including [N II] 658.3 nm), He II 468.6 nm, and [O I] 630.2 nm. At the time of the observations of this object, the line [O I] 630.2 nm happened to be strongly affected by the overlying terrestrial atmospheric emission, which unfavourably overlapped in radial velocity, so we excluded it from the analysis.

The standard ESO reduction pipeline (EsoReflex) has been applied to the raw data. Further data processing and plotting was performed using Python with modules astropy, scipy, and matplotlib. These concern the removal of bad pixels by median filtering the data cube in the XY axes (sky plane) and smoothing the spectral noise by the Savitzky-Golay filter along the wavelength axis. From the original IFU field of 22 × 14 pixels, we extracted for the analysis a square of 10 × 10 pixels that covers the whole nebula, and it is shown in the figures. The examples of the monochromatic images (i.e. integrated over the full width of a single emission line) are shown in Fig. 2. They show background emission increasing towards the right edges, which was not flat-fielded completely by the pipeline. We did not correct for this because it did not affect the morphological and kinematical modelling. Absolute flux calibration was not attempted. Instead, the line flux values needed for the model fitting were taken from the literature. In all figures we present the observational data with the sky coordinates converted to 10^{17} cm (assuming the PN distance of 8 kpc) and measured with respect to the position of the central star in order to ease the comparison with the models, where the real physical size is used. We do not present the [O III] 500.7 nm monochromatic image because it is very similar to Hα.

Previous HST observations in the Hα filter show an overall axially symmetric, elongated structure. In Fig. 1, this structure has been rotated so that it is positioned vertically. The most intense inner broad area is asymmetric, and its strongest emission is in the upper-left of the inner region. Outside of the main cylinder, near its middle, low-intensity ear-like extensions can be seen (oriented horizontally in the image), and they could be a trace of a faint equatorial ring.

Our new data confirm these features (Fig. 2 left panel) and show more than that. The IFU data revealed an intriguing pair of small and bright blobs in the [N II] 658.3 nm image (Fig. 2, middle panel); their dominant emission is axially symmetric with a weaker asymmetric component. This feature is completely absent in He II 468.6 nm (Fig. 2, right panel) and is barely visible in Hα.

We understood that neither a spherical nor an elliptical model is sufficient to describe the PN H 2-18, and we thus needed to consider the inner component. Although the elongation in the [N II] image appears jet-like, because of the high density we estimated and the low velocity, we rather describe it as bar-like or cylindrical, leaving the case open.

3. 3D model analysis

The photoionisation modelling was performed with the publicly available MOCASSIN code (Ercolano et al. 2003). We wrote supplementary codes in Python, and these concern construction of a 3D density distribution cube, calculation of the emission line shapes derived from total emissivity with the assumed velocity field and emerging from a defined pixel area on the sky, and graphical representation of the observed and modelled emissions, among others. The models we present were computed on a spatial grid of 121 × 121 × 121 points, which ensured sufficient spatial accuracy with reasonable time for simulations and image processing. We aimed at finding a model that not only was as simple as possible but also fit the images and simultaneously reproduced the line ratios and velocities.

3.1. Density structure

The components of the model discussed below are presented in Fig. 3 as a cross-section of the density distribution taken along the presumed symmetry axis. The values of the hydrogen number density are shown in the side bar, while the size of the nebula in centimetres is based on assuming the Galactic Bulge distance of 8 kpc.

The central region within a radius of 2.4×10^{16} cm was not considered in the modelling and assumed to be empty. The ionising source (central star) was assumed to be a blackbody with a temperature $T_{\rm bb}$ of 62 kK (previously, it was estimated at 52 kK).

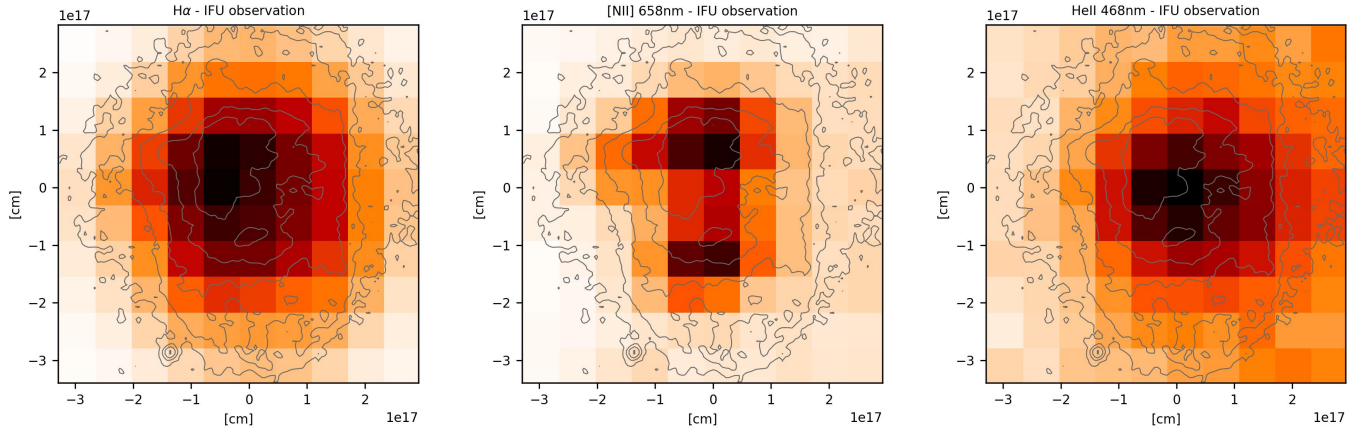

Fig. 2. Monochromatic images of ARGUS/IFU with HST contours defined in Fig. 4. The high-resolution HST image has been positioned to obtain the best agreement with the IFU images of obviously low resolution. Shown are examples of Hα, [N II] 658.3 nm, and He II 468.6 nm lines.

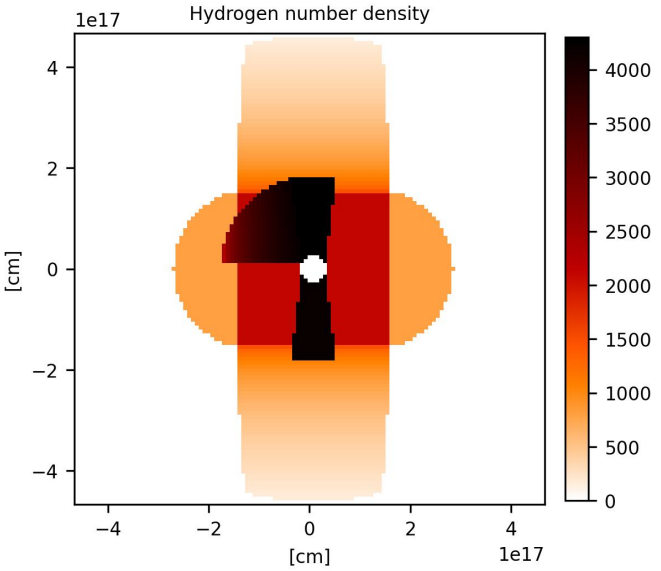

Fig. 3. Density cross-section of the assumed model. The symmetry axis is positioned vertically; all structures (except for the plume) are cylindrically symmetrical. This graph shows the true spatial dimensions of the substructures for a distance of 8 kpc. The plume is in the plane of the image and extends to $\pm 2.4 \times 10^{16}$ cm above and below it.

The main nebular body shows nearly straight edges; these are seen clearly in the vertical direction in the HST image in Fig. 1 (especially as the contours on the right side in the left panel of Fig. 4). This cannot be the ionisation boundary because we did not see the low-excitation [N II] 658 nm emission there. To reproduce this feature, we assumed a cylindrical outer structure similar to that derived previously in Gesicki et al. (2016). The difference concerns the edges, which were previously spreading outwards and had a higher density. After implementing new 3D models, we found a reasonable fit, assuming a plain cylinder fully filled with gas of density decreasing along the axis.

The nebular model structure and inclination was fine-tuned together with the velocity field – both factors provide the emission line profiles (Sect. 3.2) that verify the model. The adopted, enhanced constant density of the middle part of the main cylinder is responsible for the high intensity of the symmetric component of the Hα emission profiles. The asymmetric parts of the emission profiles of Hα and [N II] (see Figs. 5, 6) originate in the proposed inner bar and indicate that it is inclined to the plane of the sky at an angle of 40 deg (previously it was estimated at 35 deg).

The two emission blobs seen in the low-excitation line [N II] 658 nm (Fig. 2 middle panel) indicate that the ionisation front is positioned just at that location. To obtain an ionisation front at a specified position, there should be enough material between the front and the ionising source. The axial symmetry of the observed feature guided our modelling towards a narrow and dense bar-like structure. Sufficient for a rather good fit was the assumption of a constant density with a value adopted to produce the ionisation front at both far ends. Within this setup, the middle region of this bar reproduces the He II 468 nm unresolved central emission, which requires intense ionisation flux. If the [N II] 658 nm lines formed in two separate, distant blobs, the explanation of the unresolved He II 468 nm emission would need a more elaborated nebular structure.

To reproduce the asymmetric Hα image, we attached a plume to the bar-like structure. We defined this plume as a quarter of a circle having a fixed thickness and a gas density decreasing away from the symmetry axis. This structure has the same kinematics as the bar-like outflows; therefore, it is natural to place it near the axis and perpendicularly to the equatorial plane. The asymmetric plume-like structure extends to $\pm 2.4 \times 10^{16}$ cm above and below the plane of the image shown in Fig. 3. Finally, to complete the model we added an outer equatorial low-density torus.

The total nebular mass of the proposed model is 0.09 $M_\odot$; the central dense bar has a mass of 0.006 $M_\odot$, while the plume-like feature has a mass of 0.003 $M_\odot$. The chemical composition adopted for the photoionisation modelling was taken from Chiappini et al. (2009) and supplemented by the latest data from Ventura et al. (2017). The line ratios used for verification of the modelling were taken from Górny et al. (2009).

In Table 1, we compare the new model parameters with our previous analyses from 2014 and 2016 and with selected representative observational data adopted from publications. We did not perform any automated search for a best-fit model, such as the genetic algorithm used previously with spherically symmetric computations (Gesicki et al. 2006), as the model is now too complicated for that. We started with the previously found basic parameters and searched for an improvement (using trial and error, not far from the starting values) while all the time verifying the agreement with the observed data. The nebular Hβ flux

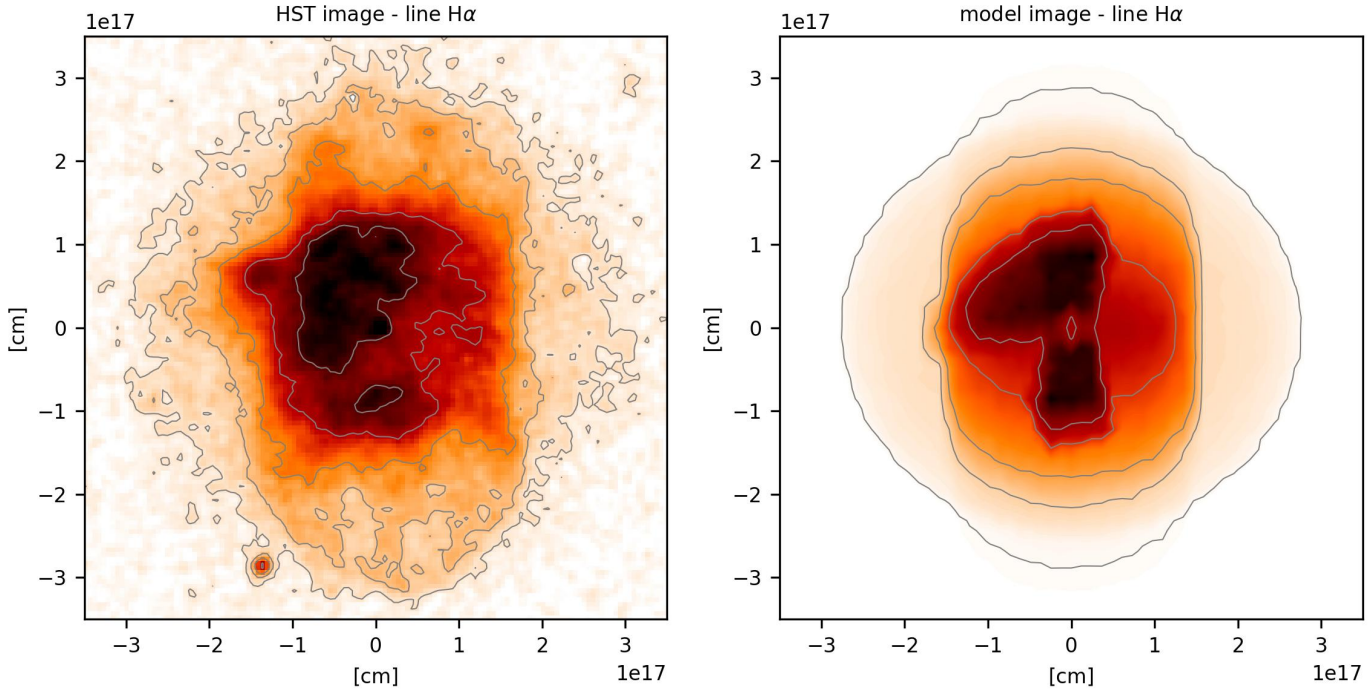

Fig. 4. Observed image in the Hα line (left panel) compared with the one obtained from the assumed model (right panel). The axes are the same as in Fig. 1. The contours (0.04, 0.09, 0.19, 0.4, 0.6 of maximum) were selected to bring out the substructures; the same contours are shown in both panels and in all other plots. For the model image, the main nebular axis is inclined to the sky plane at 40 deg, and because of a lack of background noise, the lowest contour is set at the 0.01 level.

Table 1. Parameters of the models of PN H 2-18 obtained with different codes compared with observed values.

	Modelled			Observed [a]
	2014 [b]	2016 [c]	2024	
Model version	Sphere	Ellipsoid	3D	
ion. mass [$M_\odot$]	0.27	0.051	0.096	
kin. age [k yr]	1.67	1.28	2.4	
T_{bb} [kK]	51	52	62	
$L/L_\odot$	67 000	1700	5000	
log F(Hβ)	−11.5	−11.6	−11.5	−11.5
He II 468 nm	0.078		0.058	0.05
[N II] 658 nm	0.0026	0.07	0.097	0.078
[O I] 630 nm	5×10^{-8}	8×10^{-5}	0.002	0.01
[O II] 372 nm	0.005	0.07	0.13	0.16
[O III] 500 nm	7.8	5.24	10.6	13.1
[Ne III] 386 nm	0.70		0.57	0.999
[S II] 673 nm	5×10^{-6}		0.013	0.018
[S III 631 nm	0.0002		0.009	0.01
[Cl III] 551 nm	0.007		0.081	0.0036
[Ar IV] 471 nm	0.047		0.031	0.027

Notes. The line intensities are on the scale Hβ=1. [a]Dereddened line intensities from Górny et al. (2009), [b]from Gesicki et al. (2014), [c]from Gesicki et al. (2016).

was similarly well fitted with the older simpler codes; however, details of the line ratios are significantly better reproduced with the new 3D model. This in particular concerns the strong [O III] 500 nm emission that is now excited by the higher temperature of the central star. Previously, a lower value of T_{bb} was a compromise to fit the high-excitation [O III] 500 nm simultaneously with the low-excitation [N II] 658 nm for spherical symmetry. This conflict is now resolved by the spatial distribution of the matter within the PN.

With the adopted parameters, the resulting best-fitting model produces the image in the Hα line in the plane of the sky presented in the right panel of Fig. 4, and it is compared with the HST image in the left panel. Both images are rendered as an inverted colour map to better expose the faint structures and have added contours to guide the eye. The model is not perfectly fitted, and it is not unambiguous; however, it explains all the different observed characteristics and is as simple as possible.

3.2. Velocity field

The ARGUS/IFU spectra allow for much better velocity reconstruction than previously available. However, the abundance of the data required some ingenuity to clearly present the 2D spectra and to compare the observations with models. Figure 5 shows the presentation that we designed.

The left panel shows the observations, and the right panel shows the model results. The panels cover a fragment of the sky plane, the corresponding HST image (Fig. 1) is overlaid as thin grey contours, and the coordinates are expressed in units of 10^{17} cm.

Both panels are divided into 10×10 squares representing the IFU pixels. Each square pixel shows the detailed emission profile of the Hα line, with the horizontal axis expressed in velocity units over the range ±75 km s^{-1}, and the vertical axis extends from zero to one and has been normalised to the maximum value of the whole image. To emphasise the value and direction of the velocity, we applied colour coding. As usual, red means moving away from the observer (redshifted) and blue indicates moving towards the observer. The higher the velocity, the more intense

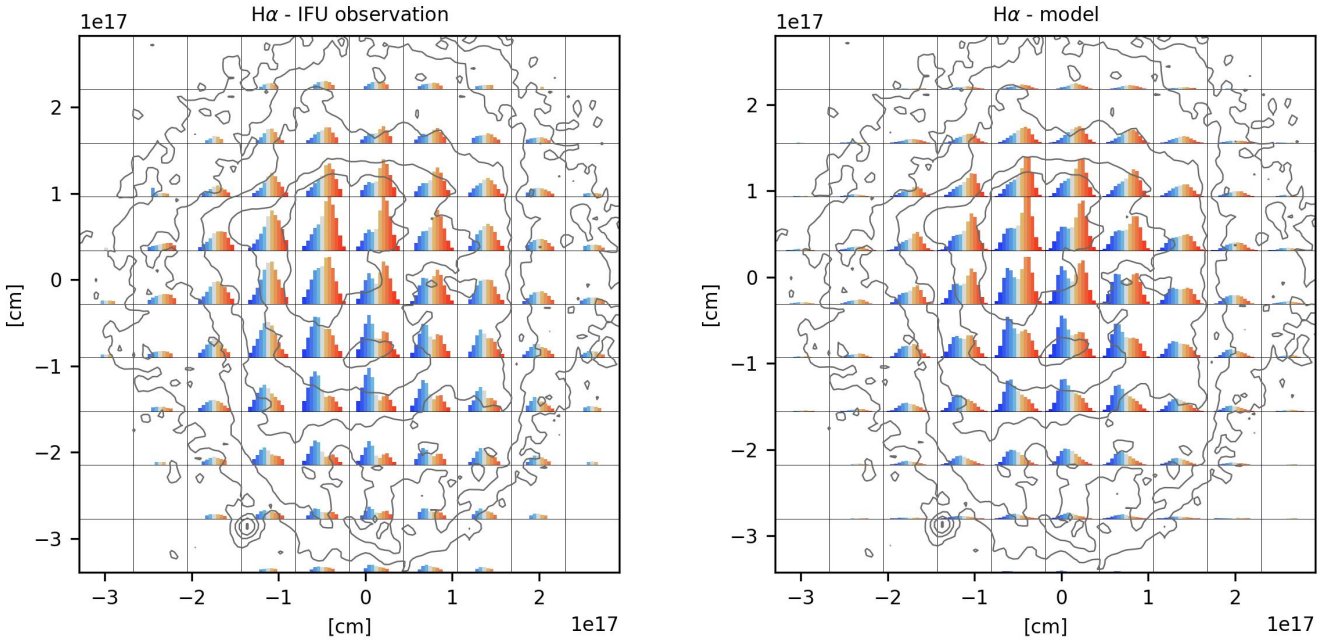

Fig. 5. Detailed emission profiles of the Hα line shown for each of the IFU pixels. The left panel shows the observed data; the right panel shows the corresponding calculated model emissions. To emphasise the value and direction of the velocity, we applied colour coding where red means gas moving away from the observer and blue indicates gas moving towards the observer, and the higher the velocity, the more intense the colour. Grey is for zero. We plotted the emission in the form of bar plots. The width of each bar is 10 km s^{-1}, and the height (intensity) has been normalised to the maximum value over the whole image. The horizontal size of each box extends to ±75 km s^{-1}; the vertical size is from zero to unity.

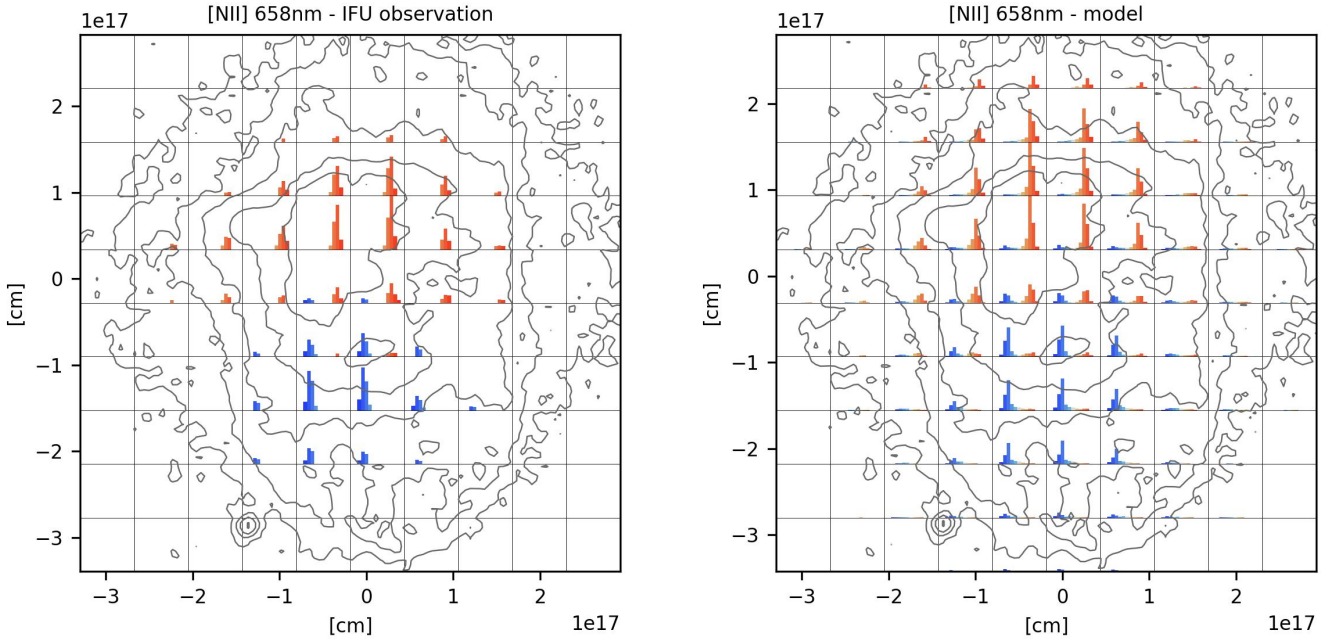

Fig. 6. Detailed emission profiles of the [N II] 658 nm line shown for each of the IFU pixels. The presentation is the same as in Fig. 5.

the colour. Grey is for zero. We plotted the emission in the form of bar plots to better show the colours. The width of each bar is 10 km s^{-1}. The grey bar is centred on zero velocity.

In the observational panel on the left, we cut off the noise at the 5% level. In the model panel on the right, we added a correction for the seeing. The seeing was below the requested 0.9 arcsec for most of the observations, except for the He II 468 nm line. When inspecting the modelled emissions integrated over the exact pixel size, it became obvious that we should allow for additional emission from some area around the given pixel that should mimic the actual seeing. We found a satisfactory fit (comparable to observations) when integration was extended by one pixel width (0.52 arcsec) around the given pixel.

In Fig. 6, the emission line [N II] 658 nm is presented in the same setup as in Fig. 5. Already at first glance, we observed that the red colour dominates in the upper half of the images, blue dominates in the lower half, and the colour in the middle row is approximately symmetric. An elongated structure can be clearly

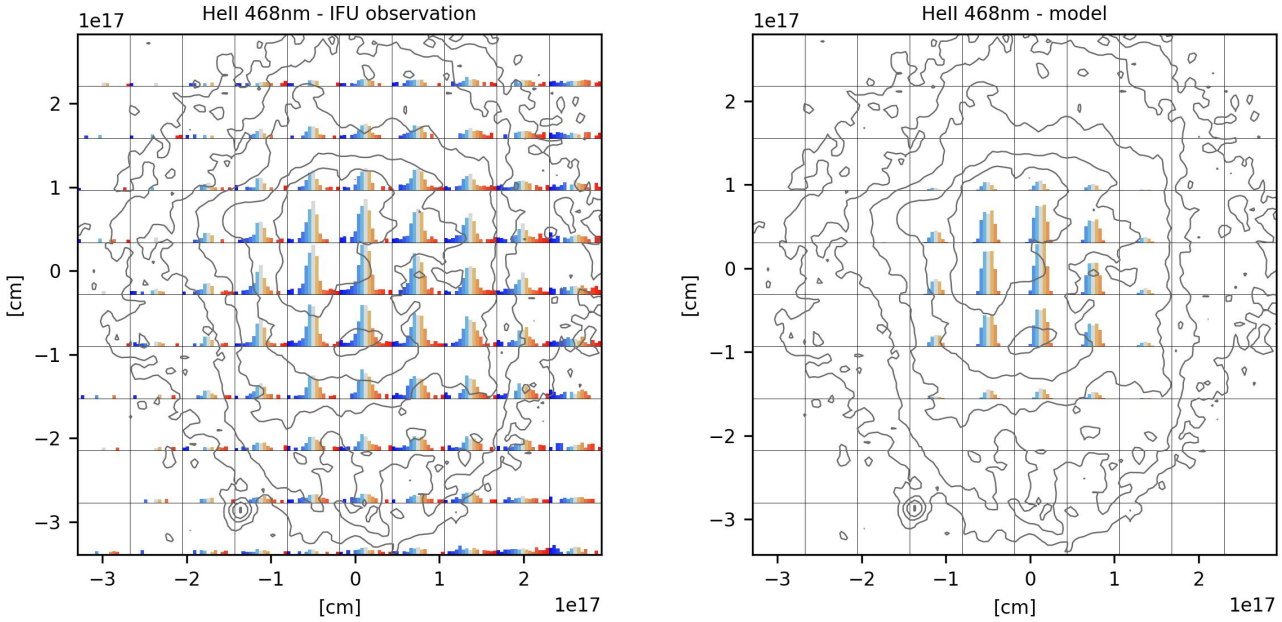

Fig. 7. Detailed emission profiles of the He II 468 nm line shown for each of the IFU pixels. The presentation is the same as in Fig. 5.

seen, and if we assume only expansion from the central source, then the upper part is directed away from us, while the lower part expands towards us. This also clarifies that the polar axis corresponds to the vertical direction in the image, something that is not obvious from the images only.

In Fig. 7 the emission line He II 468 nm is presented in the same setup as in Fig. 5. Although of lower quality, this line is unsplit and limited to the central pixels, in contrast to the [N II] emission.

The left panels of Figs. 5–7 clearly show that no extraordinary kinematics were detected within H 2-18. The velocities are within normal ranges for PNe, and there is no evidence for a fast-moving and/or collimated jet.

The data allowed us to improve on the velocity model of Gesicki et al. (2016), where the velocity was linearly increasing with radial distance. With the ARGUS data, we have spectral coverage over the whole nebula. Interestingly the velocities of the different substructures identified previously, as seen in the Hα line, are similar to each other. This suggests an isotropic velocity field. Indeed, attempts to apply different velocities to the different substructures failed to improve the fit, in agreement with this. (There may be differences at smaller scales, but we are limited by the spatial resolution of the IFU data cube.)

A radial gradient of the expansion is obviously present because the high excitation He II 468 nm line shows the lowest velocity, while the low excitation [N II] 658 nm line has the highest. A very simple relation of velocity linearly increasing with distance (homologous expansion) is not satisfactory because it makes the [N II] 658 nm line too broad in comparison with the observations. The region of the [N II] line formation should instead have a constant velocity. We adopted a velocity monotonically increasing with radial distance, starting from 10 km s^{-1} at the inner edge and reaching an asymptotic value of 60 km s^{-1} near the ends of the bar-like structure. In this way we obtained a remarkable fit to the broad, split, and asymmetrical Hα emission and simultaneously to the narrow, fast, and oppositely directed N II emissions and the spatially unresolved narrow, unsplit He II 468 nm line, as indicated by the high spectral resolution of the IFU data.

4. Discussion

4.1. New details and improved parameters

The collected IFU spectra provided new information about the Galactic Bulge nebula H 2-18. Although of a lower spatial resolution than HST, the spectra revealed a feature proposed to be a bar-like structure embedded inside the main object and co-axial with it. We call it a 'bar' rather than a 'jet' because its relatively low velocity is similar to that of the surrounding broader cylinder. The adjoining single-sided plume of ejected gas inclined to the main axis had been seen earlier in the HST images. Its kinematics are also not different from the rest of the nebula. The ear-like extensions seen in the HST image are now simply explained as being part of the outer equatorial torus.

The photoionisation modelling in 3D allowed for an improved estimation of the stellar and nebular parameters. The higher $T_{\rm bb}$ better reproduces the line ratios; the advantage of the 3D density structure is obvious in this context. The $T_{\rm bb}$ value indicates an object that is not very old – it is likely in the middle of its way towards the white dwarf cooling track. The size of this PN agrees with that, as the kinematic age is 2400 yr (derived from the mass-averaged velocity of 43 km s^{-1}, the lobes lengths of 0.15 pc, and the corrected formula of Gesicki et al. 2014).

4.2. Co-axial structures

Montoro-Molina et al. (2024) analysed the integral field spectroscopy of the PN A 58 and derived a structure of wide bipolar outflows with an embedded narrow co-axial collimated stream. Their kinematics (bipolar outflows at 280 km s^{-1}) are different from ours, but the morphology looks nearly the same (certainly excluding the plume). Montoro-Molina et al. (2024) suggested a common envelope influence. Their analyses were performed with the well-known tool SHAPE[1], which is focused on morphology and does not consider the photoionisation. A thin bar-like structure in the polar direction can be seen in the JWST image of the planetary nebula NGC 3132 (De Marco et al. 2022),

[1] https://wsteffen75.wixsite.com/website

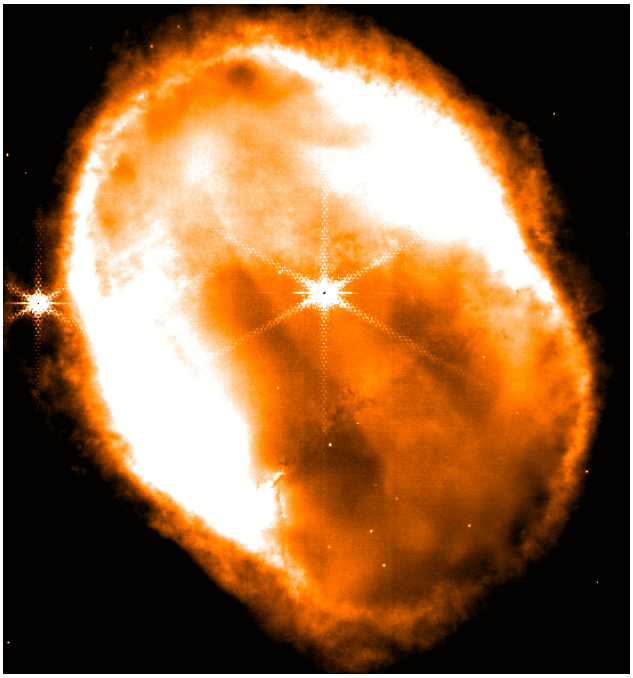

Fig. 8. Image of NGC 3132 from JWST in the filter NIRcam F187N dominated by Paα emission showing a bar-like polar structure with some similarity to that in H 2-18. The image is from De Marco et al. (2022).

shown in Fig. 8. The equatorial ring can be seen in absorption against the bar, which indicates that the bar is located inside the nebula. Both cases show that the co-axial inner and outer nebula in H 2-18 is not a unique phenomenon. (There is a thin bar-like feature in the JWST images of NGC 6720 (Wesson et al. 2024) that is a different structure. It is mainly seen as a gap and is located in the equatorial direction. It is interpreted as being the inner edges of a wide bipolar flow.)

Comparison with the published hydrodynamical calculations is hampered by the fact that very few of them show the common envelope evolution outcome on a planetary-nebula-wide scale and are rendered as images (most of them are limited to the solar radius or astronomical unit scale, and they usually present intricately shaped density cross-sections). García-Segura et al. (2018) presented a common-envelope model that is extended into the PN phase. The model assumes a pre-existing equatorial density enhancement into which the common envelope ejecta expand. It is restricted to axial symmetry with numerous simplifications and is focused on explaining bipolar shapes while skipping kinematics. Their Fig. 8 shows two examples of emission measures (a proxy for images) for complicated elongated nebulae tilted by 40 deg that show structures similar to those in H 2-18, namely, the outer barrel shape, central ellipsoidal enhancements, and symmetric extensions (ears). One of their models shows blobs of gas piled up at the symmetry axis that look similar to the symmetric N II emissions found by us. Interestingly, two separate mass ejection events are not required for the formation of both the inner and outer lobes. A follow-up study (García-Segura et al. 2022) concluded that lower mass stars will produce more elongated PNe and that the observed jets in PNe must be remnants of early phases. Both conclusions might be applicable to our case.

4.3. Low-velocity outflow

The spherical models of Gesicki et al. (2014) commonly revealed a velocity increase towards the outer nebular edge. This is in agreement with spherically symmetric hydrodynamical modelling of Schönberner et al. (2005). Here, we obtained a much more complex 3D structure, though still with a similar velocity field. We speculate that the same acceleration mechanism known from hydrodynamical models is acting here: The slowly spreading gas is accelerated and heated by the increasing ionising radiation of the gradually heating central star.

One of the conclusions of García-Segura et al. (2018) was that the inner nebulae can be ablated and photoevaporated from the excretion disc. One can expect that such a process can result in a mild acceleration of the PN. A disc wind caused by the evaporation of the photoionised gas was our interpretation of low-velocity outflows in PN M 2-29 (Gesicki et al. 2010). Recently, Icke (2022) analysed a circumstellar ring irradiated by the central star and obtained that star-driven evaporation would produce a cylindrically collimated outflow. The simple model was intended to reproduce the very elongated PN Hen 3-401. Interestingly, the cylindrical outflow appears to be relatively slow (below 10 km s^{-1} near the irradiated disc) and presumably weakly accelerated along the axis. In our Fig. 1, we did not see any obvious disc comparable to the one seen in Hen 3-401; nevertheless, some similarities exist. Our model of H 2-18 (shown in Fig. 3) has lengths comparable to Hen 3-401 and approximately twice the width (Icke 2022). The structure requires a higher density in the equatorial region, which can be treated as an approximation to a true equatorial disc or an equatorial density enhancement. Therefore, photoevaporation from this region with further photo-acceleration are plausible mechanisms shaping H 2-18.

These models are not perfect matches for H 2-18: the lobes in Icke (2022) have a low mass, while for the models of García-Segura et al. (2018), most of the common envelope mass does not reach escape velocities and remains bound. The latter model also does not present the kinematics.

Circumbinary discs in PNe have a low mass (e.g. De Marco et al. 2022) and may have difficulty explaining the dense cylindrical structure in H 2-18. A larger-sized equatorial density enhancement, however, may play a similar role.

4.4. Jets or not

Akashi & Soker (2021) have proposed that structures such as the 'ears' in H 2-18 form through polar jets, while García-Segura et al. (2018) form them by equatorial gravitational focusing. In the case of H 2-18, the ears are presumably located in the equatorial plane, so the second mechanism is more likely.

The cylindrical polar structure is more ambiguous. In García-Segura et al. (2018), it forms through expansion of the common envelope ejecta into a pre-existing equator-to-pole density gradient. Icke (2022) shows that the cylindrical nebula of Hen 3-401 can originate from an evaporating disc (possibly even from a torus) without requiring a jet. In contrast, Soker (2002) shows that cylindrical structures in PNe can form through refocused jets. The paper uses a jet velocity of 500 km s^{-1}, which could come from a main-sequence companion. Such velocities are not seen in H 2-18, nor is a jet bow shock seen, but the structure could have formed from a previous jet that is now extinct.

4.5. Binary central star

There is no direct evidence of a close binary star in the centre of H 2-18. Nevertheless, the axial symmetry of the dominant structures suggests the possibility of a binary system shaping this PN.

All the discussed hydrodynamical models require binarity. However, none appear to depend on common-envelope evolution. A wider binary interaction that avoids a common envelope can still produce an equatorial density enhancement, which may suffice. A binary (possibly even a multiple) system with a disc can be well hidden in the central unresolved dense region.

4.6. Asymmetric plume

The one-sided plume-like structure can be compared with the one observed in the PN M 2-29 (Gesicki et al. 2010). However, in H 2-18 it expands a little faster, it is seen at a different angle, and it is located inside the main nebula, although it protrudes a little out of it. It presumably has a flat structure with a nearly constant density that we proposed on the basis of the rather uniform intensity seen in the Hα image; any ploughing action of the ionisation front is not seen in the image. The mass and brightness of the plume are comparable to those of the bar, which makes it difficult to disentangle both components. This simple model does not reproduce all details, so the true shape may be more complicated. The models of García-Segura et al. (2018) show structures with a rough similarity to the plume, although point-symmetric multiplicity is lacking in H 2-18.

4.7. General aspects

In any case, the mass-loss shaping of H 2-18 has been a complex process. The high density of the inner bar or cylinder, the plume, and the lack of a detected jet put significant constraints on its evolution.

In general the understanding of physical processes that shape PNe requires accordance between observations and theory. Our method from the observations derives the density and velocity distributions that can be directly compared with theoretical models. But also very helpful in this aspect are the proxies for images and spectra that can be derived from theoretical hydrodynamical computations. In both cases the accordance that matters should be estimated in detail what is not an easy task and needs further refinement.

Acknowledgements. We thank Vincent Icke the referee for friendly and helpful comments. Help from Roger Wesson during installing and running the MOCASSIN code is gratefully acknowledged. We acknowledge financial support from the Nicolaus Copernicus University through the University Centre of Excellence 'Astrophysics and astrochemistry'. Part of this work was supported by STFC through grant ST/X001229/1. A.A.Z. also acknowledges support from the Royal Society through grant IES/R3/233287 and the University of Macquarie. This work made use of Astropy[2]: a community-developed core Python package and an ecosystem of tools and resources for astronomy (Astropy Collaboration 2022).

References

Akashi, M., & Soker, N. 2021, ApJ, 913, 91
Astropy Collaboration (Price-Whelan, A. M., et al.) 2022, ApJ, 935, 167
Chiappini, C., Górny, S. K., Stasińska, G., & Barbuy, B. 2009, A&A, 494, 591
De Marco, O., Akashi, M., Akras, S., et al. 2022, Nat. Astron., 6, 1421
Ercolano, B., Barlow, M. J., Storey, P. J., & Liu, X. W. 2003, MNRAS, 340, 1136
García-Segura, G., Ricker, P. M., & Taam, R. E. 2018, ApJ, 860, 19
García-Segura, G., Taam, R. E., & Ricker, P. M. 2022, MNRAS, 517, 3822
Gesicki, K., & Zijlstra, A. A. 2000, A&A, 358, 1058
Gesicki, K., Zijlstra, A. A., Acker, A., et al. 2006, A&A, 451, 925
Gesicki, K., Zijlstra, A. A., Szyszka, C., et al. 2010, A&A, 514, A54
Gesicki, K., Zijlstra, A. A., Hajduk, M., & Szyszka, C. 2014, A&A, 566, A48
Gesicki, K., Zijlstra, A. A., & Morisset, C. 2016, A&A, 585, A69
Górny, S. K., Chiappini, C., Stasińska, G., & Cuisinier, F. 2009, A&A, 500, 1089
Icke, V. 2022, Galaxies, 10, 53
Montoro-Molina, B., Tafoya, D., Guerrero, M. A., Toalá, J. A., & Santamaría, E. 2024, A&A, 684, A107
Schönberner, D., Jacob, R., Steffen, M., et al. 2005, A&A, 431, 963
Soker, N. 2002, ApJ, 568, 726
Ventura, P., Stanghellini, L., Dell'Agli, F., & García-Hernández, D. A. 2017, MNRAS, 471, 4648
Wesson, R., Matsuura, M., Zijlstra, A. A., et al. 2024, MNRAS, 528, 3392

[2] http://www.astropy.org